ADVANCED FUNCTIONAL MATERIALS
www.afm-journal.de

Theory-Guided Design of Non-Precious Single-Atom Catalyst for Electrocatalytic Chlorine Evolution

Kai Ma, Longfei Yang, Xiaojin Yang, Chang Zhang, Di Zhang, Linda Zhang, Li Wei, Chenliang Ye, Hao Li,* and Weijie Yang**

The chlorine evolution reaction (CER) is a crucial anodic process in the chlor-alkali industry but relies heavily on dimensionally stable anodes (DSAs) containing high-loadings of expensive noble metal oxides. To address this challenge, herein, a comprehensive big data analysis encompassing a broad set of the reported CER experiments to date, combined with catalytic volcano modeling is conducted using binding energy as a key descriptor. Leveraging these data-driven and theoretical insights, highly efficient non-precious single-atom catalysts (SACs) is designed for CER. Among them, the predicted NiN_3O-O SAC exhibited remarkable catalytic activity and selectivity, as confirmed by subsequent proof-of-concept experiments. Under acidic conditions (1 M NaCl, pH 0.9), NiN_3O-O demonstrates a low overpotential of 75 mV at 10 mA cm^{-2} and an exceptional Cl_2 selectivity of 95.8%, surpassing commercial DSA electrodes. Mechanistic investigations further reveal that the on-top oxygen (O_{ot}) in NiN_3O-O serves as the active center, with a strong preference for chloride ion adsorption over competing intermediates, which underlies its superior catalytic performance. This work establishes non-precious SACs as highly effective CER catalysts, opening a promising avenue for the development of cost-effective and efficient CER electrocatalysts.

1. Introduction

Chlorine (Cl_2) is an important industrial chemical, with an annual global production exceeding 88 million tonnDes.[1] It is widely used in pharmaceuticals, organic synthesis, and wastewater treatment.[2–4] In the chlor-alkali industry, Cl_2 is produced through the chlorine evolution reaction (CER), consuming ≈4% of the world's electricity (≈150 TWh).[5–9] Therefore, even minor efficiency improvements of the reaction can lead to substantial savings of cost and energy. Over the past half-century, DSAs composed of mixed metal oxides (MMOs) have been the most commonly used electrocatalysts in the chlor-alkali industry.[9,10] However, the high noble metal content (*e.g.*, Ru or Ir, ≈ 30 atomic%) and the significant overpotential required for CER (>90 mV) substantially increase the production cost and energy consumption of Cl_2.[4,11,12] Therefore, developing and designing highly active and low-cost CER catalysts remains a significant challenge.

Over the past decade, numerous experimental and theoretical studies have provided perspectives on developing efficient and economical CER catalysts. To evaluate the current stages of CER catalysis, we first performed a large-scale data mining from available experimental literature reported to date since 2010, as shown in **Figure 1** and Table S1 (Supporting Information). These data were also uploaded to our Digital Catalysis Platform (*DigCat*: www.digcat.org) for public use.[13] It can be

K. Ma, L. Yang, X. Yang, C. Zhang, C. Ye, W. Yang
School of Energy and Power Engineering
North China Electric Power University Baoding
Hebei 071003, China
E-mail: chenliangye@ncepu.edu.cn; yangwj@ncepu.edu.cn

K. Ma, L. Yang, X. Yang, C. Zhang, C. Ye, W. Yang
Hebei Key Laboratory of Low Carbon and High Efficiency Power Generation Technology
North China Electric Power University
Baoding, Hebei 071003, China

The ORCID identification number(s) for the author(s) of this article can be found under https://doi.org/10.1002/adfm.202525210

DOI: 10.1002/adfm.202525210

D. Zhang, L. Zhang, H. Li
Advanced Institute for Materials Research (WPI-AIMR)
Tohoku University
Sendai 980–8577, Japan
E-mail: li.hao.b8@tohoku.ac.jp

L. Zhang
Frontier Research Institute for Interdisciplinary Sciences
Tohoku University
Sendai 980-0845, Japan

L. Wei
School of Chemical and Biomolecular Engineering
The University of Sydney
Sydney, NSW 2006, Australia

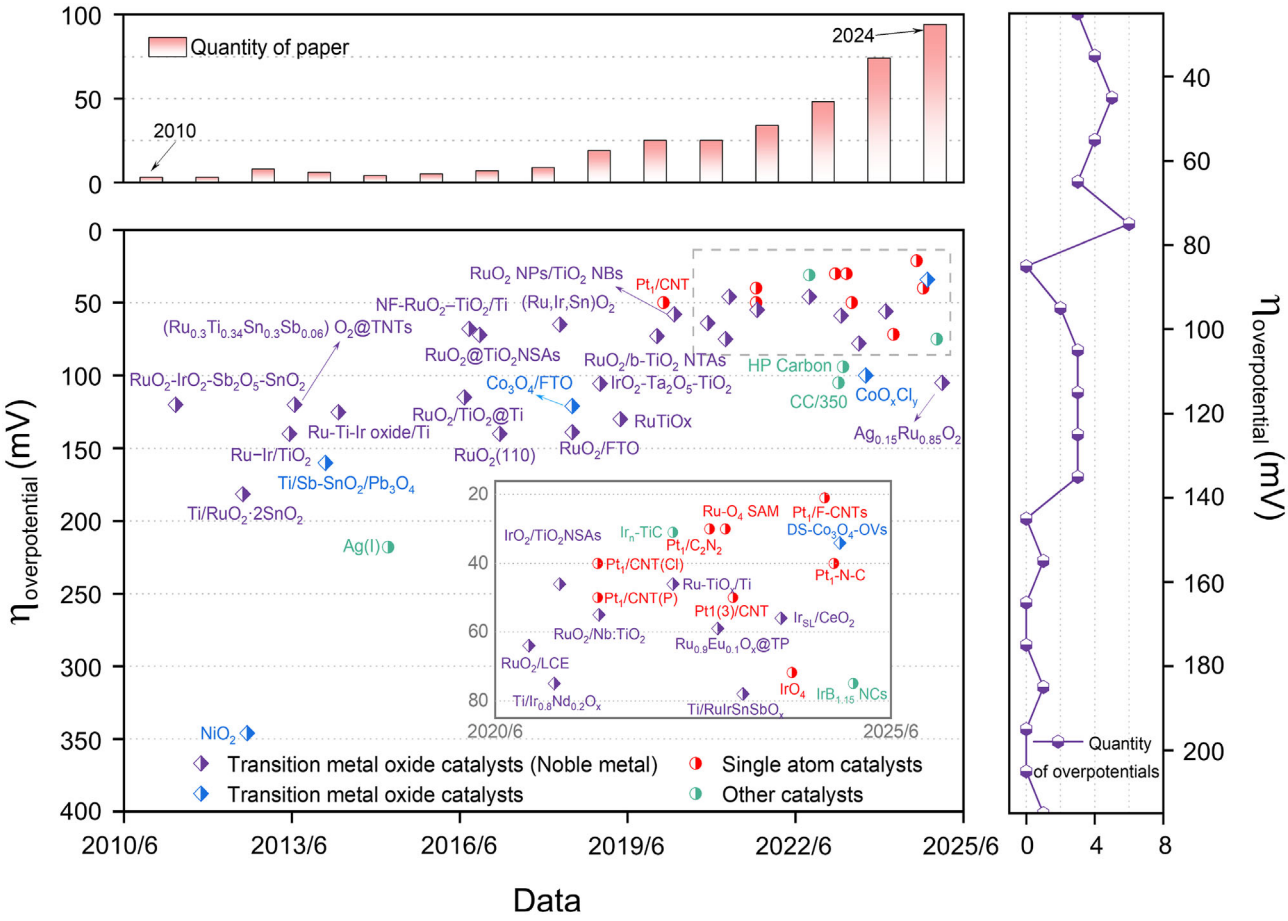

Figure 1. CER overpotentials of various catalysts reported during the past 15 years. The upper frame presents the quantity of published experimental literature for CER in the years 2010–2024. The lower frame summarizes the performance of the reported CER catalysts in terms of overpotential@10 mA cm^{-2}. The right frame summarizes the performance distribution across different CER catalysts. All relevant data are also available in Table S1 (Supporting Information) and the public Digital Catalysis Platform (*DigCat*): https://www.digcat.org/.[13]

clearly seen that most of the CER studies involve doping other transition metals (*e.g.*, Sn, Ti, Nd, and Sb) into MMOs to partially or completely replace Ru or Ir in DSA.[14–20] However, these catalysts still require a certain amount of noble metals (5%-30%) to maintain their catalytic activity.[11,19–22] In recent years, single-atom catalysts (SACs), known for their high atomic utilization efficiency, have gradually been reported for CER, such as Ru SACs supported on TiO_x foam ($Ru_1/TiO_x/Ti$)[23] and Ir SACs anchored on Ti plates (Ir-O_4/Ti).[24] Compared to traditional DSA, these catalysts exhibit significant CER activity even with extremely low noble metal loadings (0.01%–3%).[23–26] However, SACs synthesized from noble metal precursors are still considered noble metal catalysts, with relatively high costs ($83.73 g^{-1}),[24] and therefore may remain unsuitable for large-scale industrial application. Notably, a non-noble-metal single-atom system on an oxide support (Fe–Ti_4O_7) has been reported, showing markedly enhanced CER activity and scalability under seawater conditions.[27] This oxide-support study establishes the feasibility of non-noble-metal SACs for chlorine chemistry, while low-cost and efficient catalysts broadly applicable to industrial CER are still highly desired. Developing low-cost and efficient CER catalysts remains a big challenge.

CS-SACs (carbon-supported single-atom catalysts) exhibit superior performance in reactions such as the oxygen reduction, hydrogen evolution, and CO_2 reduction reactions.[28–32] This is due to their high metal-atom utilization, unique graphite structure, and tunable central metal coordination environment.[33–36] Recent experimental and theoretical studies have shown that rationally designing and adjusting the structure and coordination environment of CS-SACs to optimize the adsorption energy of reaction intermediates is crucial for enhancing their electrocatalytic performance.[25,37–40] By carefully tuning the factors such as the metal center, coordination environment, or the surrounding functional groups, the adsorption energies of reaction intermediates can be tuned, which is crucial for enhancing their electrocatalytic performance.[41–43] In recent years, various noble-metal-based single-atom configurations, such as PtN_4, RuO_4, and PtN_2C_2, have been synthesized using coordination engineering strategies.[25,26,44] According to the big-data scale illustrated in Figure 1, though most of the previously reported CER catalysts were metal oxides, the recently emerging SACs seem to generally outperform metal oxide catalysts with significantly lower overpotentials at 10 mA cm^{-2}. This suggests that SACs are a class of promising CER catalysts, which merits being further studied

due to their tunable structures and metal centers. Unfortunately, all the previously reported SACs for CER were based on noble metals with a high cost in the manufacture. Due to the highly tunable structures of SACs, one can expect that combining earth-abundant non-noble metals with CS-SACs, and rationally designing and regulating the central metal and coordination environment, holds significant potential for developing efficient and low-cost CER catalysts. Despite some recent theoretical studies on CS-SACs in CER,[45,46] to date, to the best of our knowledge, there have been no reports specifically focusing on the theoretical design, experimental validation, or mechanistic studies of non-noble metal carbon-based SACs for CER.

Motivated by the current stages and the challenges in looking for cost-effective CER catalysts, herein, we began by analyzing the potential of SACs across eight types of non-noble metal atoms and thirteen different coordination structures for CER, using spin-polarized density functional theory calculations with van der Waals corrections (DFT-D3). Stable configurations were selected based on their binding and formation energies. A volcano model of CER activity was derived based on the reaction intermediates, and the CER catalytic activities of different structures were predicted. In addition, a promising SAC for CER, namely the NiN_3O-O (with an axial on-top O (O_{ot}) structure), was identified in combination with the Pourbaix diagram under CER operating conditions. Subsequently, NiN_3O-O SACs with an axial O_{ot} structure were designed and synthesized based on the computational screening results. Our follow-up proof-of-concept experiments showed that, in acidic media containing 1.0 M NaCl, NiN_3O-O exhibited excellent CER activity, with an overpotential of only 75 mV at a current density of 10 mA cm^{-2}, outperforming commercial DSA. Additionally, NiN_3O-O demonstrated high CER selectivity across various current densities, nearly comparable to that of DSA catalysts (≈95%). Finally, the reaction pathway and the origin of the superior CER activity and selectivity of NiN_3O-O were illustrated by detailed mechanistic analyses. Combining the catalysis theory with proof-of-concept experimental validation, this work experimentally validates the feasibility of non-noble-metal SACs for CER. Our work expands the scope of CER research and opens a promising avenue for the rational design of highly active and cost-effective CER catalysts.

2. Results and Discussion

2.1. Structural Modeling and Stability Analysis

So far, numerous experiments have reported the successful synthesis of 3*d* transition metals (*e.g.*, Ti, V, Cr, Mn, Fe, Co, Ni, and Cu) as the metal centers in CS-SACs.[47,48] Previous studies have shown that the binding stability of these 3*d* transition metals with CS-SACs is superior to those of 4*d* and 5*d* transition metals due to their smaller atomic radius.[49] Therefore, to analyze the CER performance of non-noble metal SACs, herein, we selected eight 3*d* transition metals as the candidate metal centers. In addition, we introduced different heteroatoms (N or O) into CS-SACs to modify the local coordination environment of the metal center, thereby adjusting the adsorption strengths of the reaction intermediates at the catalyst.[50–52] For each system, we created 13 structural models ($TMO_xN_yC_z$) with varying coordination environments of nitrogen and oxygen. The number of neighboring oxygen, nitrogen, and carbon atoms around the central metal atom ranged from 0 to 4 (**Figure 2a**; Figure S1, Supporting Information). In total, we constructed 104 non-noble metal based CS-SACs.

To screen out promising CER catalytic structures, we performed DFT calculations for each structure, using the RPBE functional to describe exchange–correlation interactions, as it provides more reliable adsorption energies on transition-metal surfaces by mitigating the overbinding tendency of PBE(refer to Note S1, Supporting Information). With the steps shown in Figure 2b. Considering the stability and ease of synthesis of the catalyst structures, $TMO_xN_yC_z$ should exhibit strong metal-support interactions. Therefore, we used formation energy (E_f) and binding energy (E_b) as the criteria to evaluate the structural stability and ease of synthesis of $TMO_xN_yC_z$ (refer to Note S2, Supporting Information).[49,53] First, we compared the formation energy to zero to assess whether the catalyst's formation is thermodynamically favorable, where a thermodynamically favorable formation is associated with strong interactions between the metal and the substrate. Second, by calculating the binding energy of the metal atom on the graphene substrate, we can measure the anchoring strength of the metal atom. Comparing the binding energy to the metal cohesive energy helps determine whether the metal atom is easy to aggregate.

The computational results show that the stability of the same metal atom varies significantly with different coordination environments (Figure S2, Supporting Information). For all metal atoms, as the number of carbon coordination atoms increases, the thermal stability decreases, such as in the C_4 and C_3N coordination. Furthermore, as the number of nitrogen coordination atoms increases, the formation energy of the catalyst structure becomes more negative. It indicates that nitrogen doping significantly enhances the thermodynamic stability of the double vacancies. The results of this study (Table S2, Supporting Information) are generally consistent with the computational findings by Yang et al.[53] For the binding energy, it becomes less stable as the number of doped oxygen atoms increases (Tables S2 and S3, Supporting Information). This indicates that an increase in the coordination of O will weaken the anchoring strength of the metal on the catalyst surface. Herein, most of the metal atoms in the N_4, N_3O, and N_3C coordination structures are identified as stable. This indicates that the N_4, N_3O, and N_3C coordination structures in the graphite substrate provide a sufficiently strong anchoring effect to prevent metal aggregation. Finally, based on the formation energy and aggregation characteristics, 37 potential stable configurations were identified out of the 104 considered structures.

2.2. Screening and Analysis of Highly Active Structures

Previous literature has shown that most catalysts undergo CER through a two-electron Volmer-Heyrovsky mechanism.[23–26,54–56] In this process, chloride ions are adsorbed at the active site and transfer electrons to form reaction intermediates, which are then directly combined with chloride ions in the electrolyte to generate Cl_2. DSA materials, such as RuO_2, $RuTiO_2$, and IrO_2, have been proposed to use Cl and OCl* as the reaction intermediates in CER.[57–60] Theoretical calculations indicate that there are two possible reaction pathways for different intermediates:

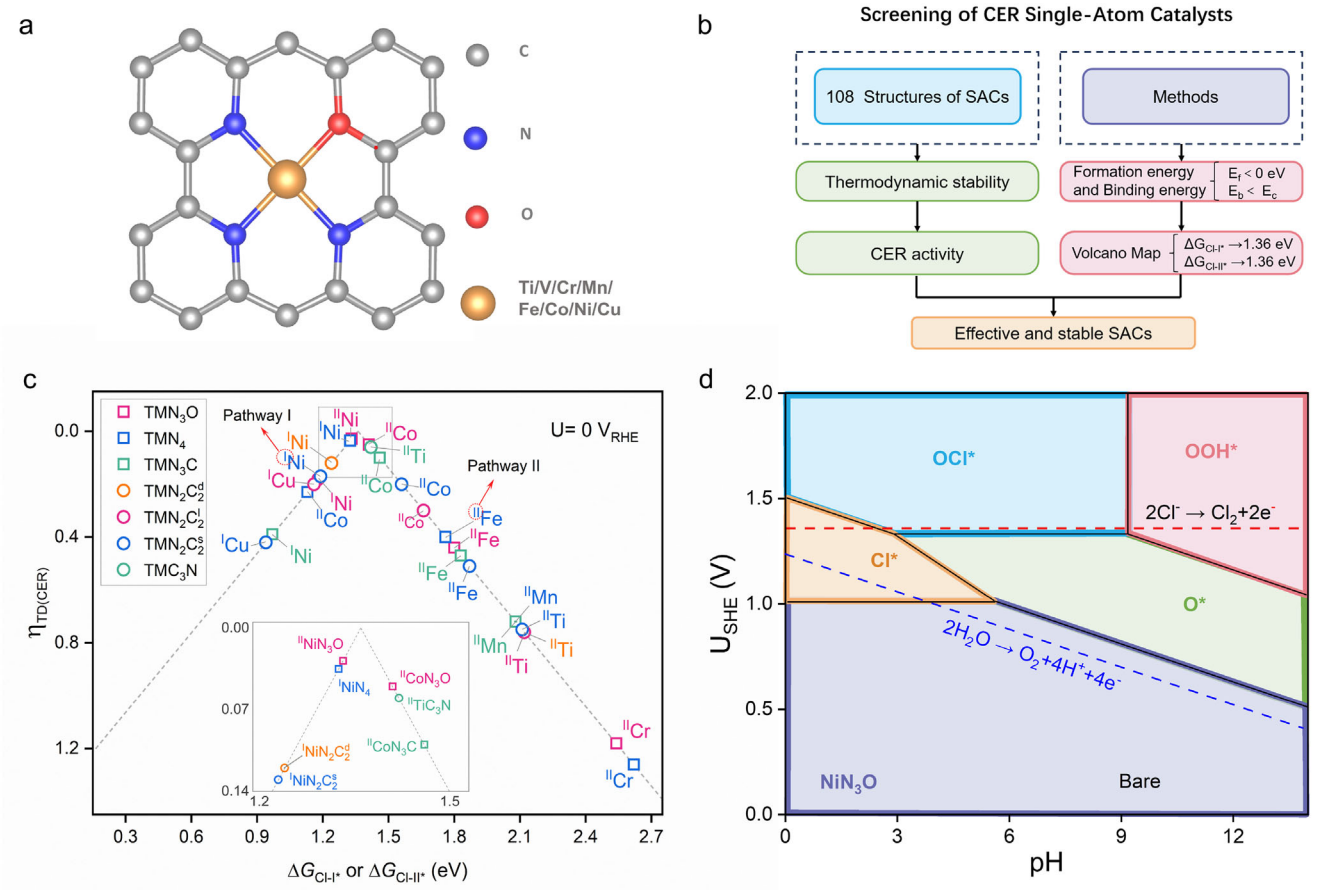

Figure 2. Computational screening of non-noble metal-based SACs for CER. a) Schematic illustration of a $TMO_xN_yC_z$ structure using TMN_3O as an example, where C, O, N, and TM atoms are represented in gray, blue, red, and golden-brown, respectively. b) Illustration of the screening workflow of CER catalysts. c) The derived volcano model predicting the CER overpotentials as the function of reaction descriptors. ΔG_{Cl-I^*} describes Pathway I, which uses ΔG_{Cl^*} as the reaction descriptor. ΔG_{Cl-II^*} describes Pathway II, which uses ΔG_{OCl^*}-ΔG_{O^*} as the reaction descriptor (for more details, please refer to Note S3, Supporting Information). d) Pourbaix diagram of the standard hydrogen electrode potential (U_{SHE}) versus pH for NiN_3O in equilibrium with H^+, Cl^-, and H_2O at T = 298 K. The two dashed lines represent the equilibrium potential of CER (U_{CER} = 1.36 V vs SHE) and OER (U_{OER} = 1.23 V – 0.0592 * pH), respectively. Black solid lines represent the phase boundary where two adsorbate species exist in equilibrium.

i) Chlorine can directly adsorb onto the exposed active site (*) to form a Cl* intermediate, leading to CER; ii) The active site is first oxidized at the anode to form an O_{ot} structure, which then acts as a new active site to adsorb chloride, forming an OCl* intermediate, ultimately resulting in CER. The two reaction pathways are shown in the following Equations (1–5):

Pathway I (Cl*):

$$* + Cl^- (aq) \rightarrow Cl* + e^- \quad (1)$$

$$Cl* + Cl^- (aq) \rightarrow * + Cl_2 (g) + e^- \quad (2)$$

Pathway II (OCl*):

$$* + H_2O \rightarrow O* + 2H^+ + 2e^- \quad (3)$$

$$O* + Cl^- (aq) \rightarrow OCl* + e^- \quad (4)$$

$$OCl* + Cl^- (aq) \rightarrow O* + Cl_2 (g) + e^- \quad (5)$$

Therefore, we established the adsorption structures of Cl*, O*, and OCl* for the 37 identified stable SAC configurations (Figure S3, Supporting Information). According to the *Sabatier* principle, a catalyst that moderately adsorbs chloride has higher CER activity compared to catalysts that bind chloride too strongly or too weakly.[61] Therefore, we used the calculated free energies of the two intermediates as descriptors to derive an activity volcano model for the $TMO_xN_yC_z$ catalysts, as shown in Figure 2c. For the two reaction pathways and reaction intermediates with different structures, different thermodynamic overpotentials will be caused. Therefore, we chose the reaction pathway that leads to a lower thermodynamic overpotential as a reference. At the equilibrium potential of 0 V versus reversible hydrogen electrode (RHE), an adsorption free energy of the reaction intermediates closer to 1.36 eV suggests a higher CER performance (with the overpotential closer to 0 V). The thermodynamic overpotential for CER can be defined as ΔG divided by the elementary charge at zero overpotential (*i.e.*, $\eta_{td(CER)} = \Delta G/e$).[62] As can be seen in Figure 2c, the structures such as NiN_3O, NiN_4, CoN_3O, and TiC_3N are close to the apex of the volcano model. To identify the most promising

CER catalysts, this study mainly focused on the candidate structures with the lowest overpotential. The structure at the apex of the volcano model is NiN_3O, whose adsorption free energy through Pathway II (O_{ot} site) is $\Delta G_{Cl\text{-}II^*} = 1.33$ eV, resulting in a thermodynamic overpotential of only 28.0 mV (Table S4, Supporting Information). This indicates that the NiN_3O structure exhibits excellent performance in CER through Pathway II at the O_{ot} site.

The Pourbaix diagram was further constructed using an ab initio constrained thermodynamics approach (Figure 2d), which can explore information about the most thermodynamically stable structure on the surface of the catalytic structure at a given applied bias U and pH values.[63,64] To further analyze the specific performance of the NiN_3O configuration in catalyzing CER, we calculated the adsorption free energies (ΔG) of potential adsorbates (OCl*, Cl*, OOH*, O*, and OH*) and constructed a Pourbaix diagram based on these data (Figure 2d; Figures S4 and S5; Note S4, Supporting Information). This was done to explore information about the most stable surface structure of this configuration under a given applied voltage (U) and pH.[63] In the standard hydrogen electrode (SHE) scale, CER is independent of pH, and thus it appears as a horizontal line at the equilibrium potential of 1.36 V versus SHE. At the anode, CER is typically accompanied by the oxygen evolution reaction (OER) as a side reaction.[57,65] As a competing reaction, the equilibrium potential of OER starts at $U_{SHE} = 1.23$ V (pH 0), characterized by a line with a slope of -59 mV pH^{-1}.[66] Notably, under neutral and acidic conditions, the central Ni site in NiN_3O readily adsorbs Cl at low potentials ($U_{SHE} > 1.05$ V), which makes it difficult to desorb Cl adsorbed at CER equilibrium potentials, resulting in a high thermodynamic overpotential of up to 0.35 V. This indicates that CER is unlikely to occur for NiN_3O through Pathway I. In addition, for pH > 9.2 and U_{SHE} >1.34 V, the HOO* adsorption structure becomes optimally preferred in energy, indicating that the HOO* intermediate acts as a precursor state for OER under this condition. At slightly higher potentials ($U_{SHE} > 1.33$ V) and pH < 9, chloride ions moderately adsorb onto the O_{ot} site, forming a stable OCl* intermediate. However, forming the OCl* intermediate requires the precursor O* (*i.e.*, the O_{ot} site) from OER, which leads to unnecessary steps in the occurrence of CER and may thereby reduce the kinetic performance at the beginning of the reaction.[67] Furthermore, at the CER equilibrium potential of 1.36 V (Figure S6, Supporting Information), the formation of O* requires OH* precursors, but the formation of OH* precursors still requires an overpotential of 0.184 V, which is higher than the calculated CER overpotential of 28 mV. Therefore, the NiN_3O-O with an axial O_{ot} structure (Figure S7, Supporting Information) can be directly adopted as the ideal catalytic structure for CER. Combined with the low thermodynamic overpotential and two-electron mechanism of CER generated at the O_{ot} site, its kinetic and thermodynamic performance can be maximized. In addition, the formation energy of the NiN_3O-O structure was calculated to be -2.0 eV (Table S5, Supporting Information), which indicates that the structure is thermodynamically more stable than NiN_3O (*i.e.*, the bare surface) itself under oxidizing conditions. The binding energy of NiN_3O-O is -4.9 eV, which is more negative (*i.e.*, more stable) than the atomic cohesion energy of Ni, which further supports that the NiN_3O-O structure is feasible. We also note that these results indicate that even without the formation of an adsorbed O_t after synthesis, the NiN_3O-O structure can still easily form during CER conditions via H_2O activation due to its strong-binding nature of the Ni-site of NiN_3O. But naturally, under an oxygen-rich synthetic condition, we can expect that the NiN_3O-O structure, which is ideal for CER via the Pathway II, can easily be synthesized due to its higher stability than NiN_3O itself.

2.3. Proof-of-Concept of the Theoretical Calculations

Based on the screening results above, we performed proof-of-concept experiments by synthesizing the NiN_3O-O catalysts using a hydrothermal–annealing route adapted from our previous NiN_4-O protocol,[68] with modifications in the oxidation of carbon black, hydrothermal conditions, and low-temperature annealing to stabilize the NiN_3O–O coordination structure (see Note S5, Supporting Information). Here, oxidized carbon black (OCB), used as a carrier to provide a graphite structure, was prepared by dispersing carbon black (2 g) in 40 mL nitric acid solution (7 mol L^{-1}) and stirring for 1 h, followed by hydrothermal treatment at 120 °C for 24 h. After cooling, the solids were collected, dried at 80 °C under vacuum, and used for catalyst synthesis. Specifically, 120 mg of OCB was dispersed in 10 mL H_2O and stirred for 1 h, then 220 mg of pyridine-2,5-dicarboxylic acid and 38.38 mg of nickel nitrate were sequentially added with continued stirring (1 h and 30 min, respectively). The mixture underwent a hydrothermal reaction at 180 °C for 6 h, and the resulting solids were collected, vacuum-dried at 80 °C, and annealed at 300 °C for 1 h under a 0.1 L·min^{-1} N_2 flow (99.999%) with a heating rate of 2.1 °C·min^{-1}. The obtained NiN_3O–O catalyst exhibited a Ni loading of 5.17 wt.% (ICP-OES, Table S7, Supporting Information), and samples from multiple batches showed consistent electrochemical performance, indicating good reproducibility and stability of the synthesis method. The more detailed synthesis procedure is provided in Note S5 (Supporting Information), and the resulting sample is denoted as NiN_3O–O (Note S5, Supporting Information). Using scanning electron microscopy (SEM) and transmission electron microscopy (TEM), we closely observed the physical morphology of NiN_3O-O. Notably, NiN_3O-O exhibits a well-defined spherical structure, with its surface covered by a thin, complex 3D nanostructure (Figure S8a,b, Supporting Information). Additionally, TEM analysis revealed ordered lattice fringes in NiN_3O-O, corresponding to the (002) plane of graphite carbon (Figure S8c, Supporting Information). The elemental mapping of the nanosheets shows that these elements are uniformly distributed across the surface of the sample, with no obvious Ni nanoparticles or clusters detected (**Figure 3a**). Atomically dispersed Ni can be directly observed by aberration correction (AC) HAADF-STEM (Figure 3b). The HAADF-STEM image of NiN_3O-O shows scattered bright spots, confirming that Ni atoms are dispersed on the carrier OCB. The characterization of NiN_3O-O and the OCB support was performed using a high-power X-ray diffractometer equipped with Co Kα radiation and a DXR Raman spectrometer. The X-ray diffraction (XRD) patterns of both materials exhibited two distinct diffraction peaks. These peaks correspond to the graphite (002) and (111) planes, which is consistent with TEM measurements (Figures S8c and S9a, Supporting Information). This indicates that the synthesis did not alter the physical structure of the carbon black. Notably,

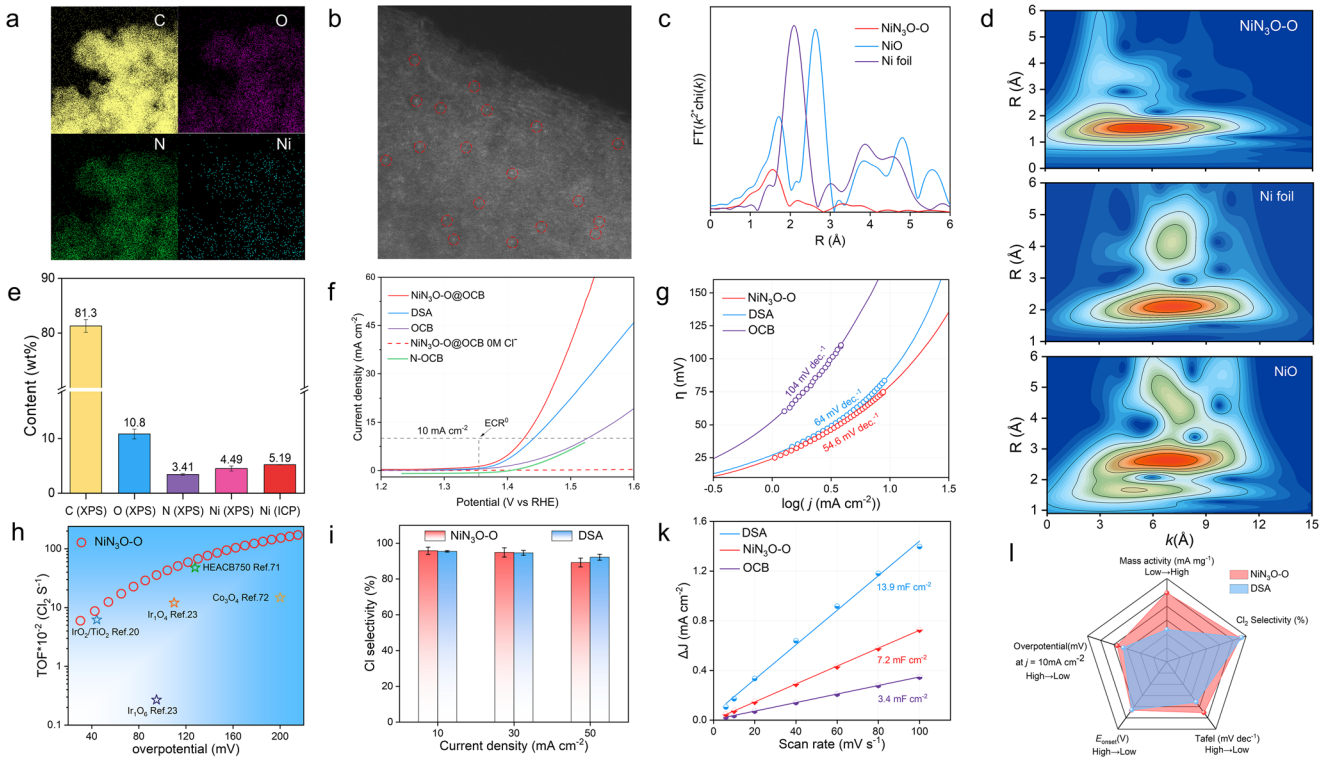

Figure 3. a,b) EDS elemental mappings and AC HAADF-STEM image of NiN_3O-O. Single atoms are highlighted by red circles. c) k^2-weight FT-EXAFS curves of NiN_3O-O, NiO, and Ni foil at Ni K-edge. d) WT-EXAFS plots of NiN_3O-O, NiO, and Ni foil, respectively. e) Elemental content of NiN_3O-O obtained from XPS and ICP-AES. f) Polarization curves of NiN_3O-O, DSA, and OCB in 0.1 M H_2SO_4 + 1 M NaCl solution were obtained with a scan rate of 10 mV s^{-1} and an electrode rotation speed of 1600 rpm. The polarization curve of the NiN_3O-O catalyst measured in 0.1 M H_2SO_4 is also shown. Note: the measurement of DSA did not require electrode rotation. All polarization curves were corrected with 95% *iR* compensation. g) Tafel plots of NiN_3O-O, DSA, and OCB. h) Turnover frequency (TOF) of the NiN_3O-O calculated based on the loaded Ni atoms at different overpotentials along with some recently reported promising CER catalysts. i) Selectivity of NiN_3O-O and DSA at different current densities. k) The plot of current density at 1.0 V versus RHE against the scan rate. The slope is the double layer capacitance (C_{dl}). l) Comparison of the performance parameters of NiN_3O-O and DSA.

no diffraction peaks associated with nickel species were observed in the XRD pattern of NiN_3O-O, suggesting that no nickel clusters were formed. The Raman spectra of both NiN_3O-O and OCB exhibited two prominent peaks: the D band (≈1344 cm^{-1}), representing the degree of disorder, and the G band (≈1581 cm^{-1}), related to the degree of graphitization.[69] Furthermore, the intensity ratio (Figure S9b, Supporting Information) of the D band to the G band (I_D/I_G = 1.012) for the catalyst was higher than that for OCB (I_D/I_G = 1.007), which indicates the sample has a higher degree of disorder and defects compared to oxidized carbon black. X-ray photoelectron spectroscopy (XPS) spectral composition analysis (Figure S10a, Supporting Information) showed that Ni, O, N, and C elements existed in the material, and no other impurities were detected. The Ni 2p XPS spectra of the NiN_3O–O catalyst (Figure S10b, Supporting Information) display a broad Ni $2p_3/_2$ envelope centered at ≈856 eV and a higher-binding-energy feature at ≈861–862 eV, which is characteristic of the shake-up satellite. Due to the relatively low Ni content, the spectrum exhibits a weak signal-to-noise ratio and partially overlapped features, making detailed deconvolution (e.g., Ni^{2+} vs Ni^{3+}) challenging. No distinct component is observed around ≈852.6 eV, suggesting that metallic Ni^0, if present, is below the detection limit. Inductively coupled plasma optical emission spectroscopy (ICP-OES) quantitative measurements indicated that the Ni content in the sample was approximately 5.17 wt.% (Table S7, Supporting Information). This value is basically consistent with the XPS measurement of 4.49 wt.% (Figure 3e). The average contents of C, O, and N in NiN_3O-O were 81.3, 10.8, and 3.41 wt.%, respectively.

To determine the precise structure of the sample, we used X-ray absorption near edge structure (XANES) and extended X-ray absorption fine structure (EXAFS) to study the electronic state and local coordination environment of NiN_3O-O. The absorption edge position of NiN_3O-O was slightly higher than that of NiO (Figure S9c, Supporting Information), indicating that the valence state of Ni in NiN_3O-O was slightly higher than Ni^{2+}. Additionally, Fourier-transformed k^2-weighted EXAFS (FT-EXAFS) analysis revealed geometric information about NiN_3O-O at the atomic level. NiO and Ni foil exhibited prominent peaks at 1.69 and 2.08 Å, respectively, corresponding to the first-shell coordination of Ni-O and Ni-Ni (Figure 3c). In contrast, the FT-EXAFS spectrum of NiN_3O-O did not show a Ni-Ni peak; instead, a main peak appeared at 1.56 Å, attributed to the closest coordination distances of Ni-O and Ni-N bonds.[69] This suggests that Ni atoms are isolated and anchored on the OCB surface, consistent with the HAADF-STEM image in Figure 3b. Least-squares fitting of the EXAFS curves was used to determine the structural parameters of Ni in NiN_3O-O and Ni foil. Figure S9d,e (Supporting

Information) shows the R-space fitting and model-based EXAFS fitting, respectively. The fitting results (Table S8, Supporting Information) clearly indicate that the main peak at 1.56 Å arises from the first-shell coordination of Ni–N and Ni–O, with a total coordination number of Ni–O/N of 4.6 ± 0.4. Beyond EXAFS, complementary evidence supports the proposed NiN_3O-O configuration: O 1s XPS shows a distinct component at 531.3 eV (Figure S11, Supporting Information), consistent with Ni–O coordination, and DFT calculations indicate a low formation energy for the NiN_3O-O motif (−2.05 eV; Figure S12, Supporting Information), suggesting that this configuration is thermodynamically favorable under our synthesis conditions. To determine the atomic arrangement of backscatters in *R*-space and *k*-space, we performed wavelet transform (WT) analysis of the EXAFS spectra (Figure 3d). In the WT-EXAFS spectra of NiN_3O-O and NiO, a maximum intensity contour due to Ni-O scattering was observed at 5.2 $Å^{-1}$. Compared to the WT signal of Ni foil, the intensity peak in NiN_3O-O was shifted away from that of Ni foil, and no Ni-Ni coordination was observed, indicating that the isolated Ni atoms were anchored by O and N atoms.

First, we evaluated the electrocatalytic performance of NiN_3O-O, commercial DSA, and the OCB support using a rotating ring-disk electrode (RRDE) and H-type electrolytic cell. Linear sweep voltammetry (LSV) was used to record the polarization curves of NiN_3O-O, commercial DSA, OCB and the N-doped OCB control (N-OCB, prepared without the Ni precursor). Unless otherwise specified, all performance tests were conducted in 1 M NaCl (0.1 M H_2SO_4) solution and other electrochemical test methods are shown in Note S6 (Supporting Information). As shown in Figure 3f, the LSV curve of NiN_3O-O initially rises steeply, with an onset potential (E_{onset}) of 1.36 V (defined as the potential required to reach a current density of 3 mA cm^2), lower than those of commercial DSA at 1.38 V and OCB at 1.44 V. This indicates that NiN_3O-O has better catalytic activity compared to commercial DSA and OCB. The N-OCB control exhibits negligible CER activity and does not reach 10 mA cm^{-2} within the scanned window (up to ≈1.55 V vs RHE), showing that the N-doped carbon support alone contributes minimally under our conditions. The overpotential required to achieve a current density of 10 mA cm^{-2} is another important parameter for evaluating CER performance. At a current density of 10 mA cm^{-2}, NiN_3O-O exhibited an overpotential of only 75 mV, which is lower than that of commercial DSA (91.3 mV) and most of the reported noble metal oxide catalysts (Table S1, Supporting Information). Within this potential range, the production of Cl_2 can be confirmed by reduction at the platinum ring (Figure S13, Supporting Information). The Tafel plots of NiN_3O-O, commercial DSA, and OCB are shown in Figure 3g. In the overpotential range of 25–75 mV, the Tafel slope for NiN_3O-O was 54.6 mV dec^{-1}, which is lower than that of DSA (64 mV dec^{-1}) and OCB (102 mV dec^{-1}), indicating that CER proceeds faster on NiN_3O-O compared to commercial DSA and OCB. The Tafel slope of 54.6 mV dec^{-1} suggests that CER on NiN_3O-O likely follows the Volmer-Heyrovsky mechanism, which is consistent with DFT calculations.[70–73] The turnover frequency (TOF) value of NiN_3O-O was calculated based on the number of Ni atoms loaded. At an overpotential of 100 mV, the TOF was 0.51 s^{-1}, which is higher than some previously reported catalysts(Figure 3h).[21,23,74,75]

Since both CER and OER occur at the anode, and OER (E_{OER} = 1.23 V vs RHE) has a lower potential than CER (E_{CER} = 1.36 V vs RHE), it is necessary to consider the selectivity of the catalyst for Cl_2. In the absence of sodium chloride (0 M NaCl), NiN_3O-O did not show a significant current signal (Figure 3f), suggesting that the current signal observed at this electrode came from CER rather than OER. The selectivity of NiN_3O-O and commercial DSA at different current densities was determined by iodometric titration. The selectivity of NiN_3O-O reached 95.8%, almost identical to that of commercial DSA (95.4%), confirming its good selectivity against Cl_2 (Figure 3i). A comparison of CER performance data (Figure 3l and Table S9, Supporting Information) shows that NiN_3O-O performs better than some previously reported DSA electrodes.[11,23,25,76] Further electrochemical studies of NiN_3O-O, commercial DSA, and OCB using cyclic voltammetry were performed to analyze their electrochemical double layer capacitance (C_{dl}) at different potential sweep rates to determine their electrochemically active surface area (ECSA). C_{dl} and ECSA (Figure 3k; Figure S17, Supporting Information) of NiN_3O-O were 7.2 mF cm^{-2} and 180 cm^2, respectively, higher than OCB's 3.4 mF cm^{-2} and 85 cm^2, but lower than commercial DSA's 13.9 mF cm^{-2} and 347 cm^2. Interestingly, the ECSA trends for NiN_3O–O and commercial DSA are opposite to the polarization curve results shown in Figure 3f. This apparent discrepancy can be rationalized by considering that the current density (j) at a given potential is determined by both the intrinsic activity (a) of each active site and the total electrochemically active surface area (ECSA), according to $j \propto a \times ECSA$. Although NiN_3O–O exhibits a smaller ECSA compared to commercial DSA under identical conditions, its significantly higher intrinsic activity per active site results in a larger overall current density. This finding highlights that the superior catalytic performance of NiN_3O–O primarily originates from its high intrinsic activity rather than merely from the total active surface area, and preliminary stability evaluation (Figure S15, Supporting Information) demonstrates that NiN_3O–O exhibits good stability. Nevertheless, its relatively low synthesis cost (10.82 USD g^{-1}), which is only ≈3.3% of the market price of the RuO_2 and IrO_2 catalyst coatings in DSA electrodes (327.82 and 366.39 USD g^{-1}, respectively), suggests a potential market advantage for NiN_3O–O in practical applications if stability can be further enhanced (Table S10, Supporting Information).

2.4. Subsequent Mechanistic Analysis

To further elucidate the reaction mechanism and the high CER selectivity of NiN_3O-O, we conducted detailed mechanistic analyses using DFT calculations. Our calculations have shown that the O_{ot} site in the axial structure of NiN_3O-O can adsorb Cl, thus facilitating the CER. However, considering possible reaction pathways (**Figure 4a**), CER can also occur at the bottom site of Ni of the NiN_3O-O (hereafter referred to as NiN_3O-O', where metal Ni directly serves as the reaction site). Additionally, to compare with commercial DSA catalysts, we constructed a model of the rutile RuO_2 (110) surface (Figure S16, Supporting Information), which includes two types of Ru sites: one is the bridged Ru site (Ru_{bri}) with saturated coordination, and the other is the five-coordinated unsaturated Ru site (Ru_{cus}).[77,78] Previous studies have indicated that, for the typical rutile RuO_2 (110), the CER

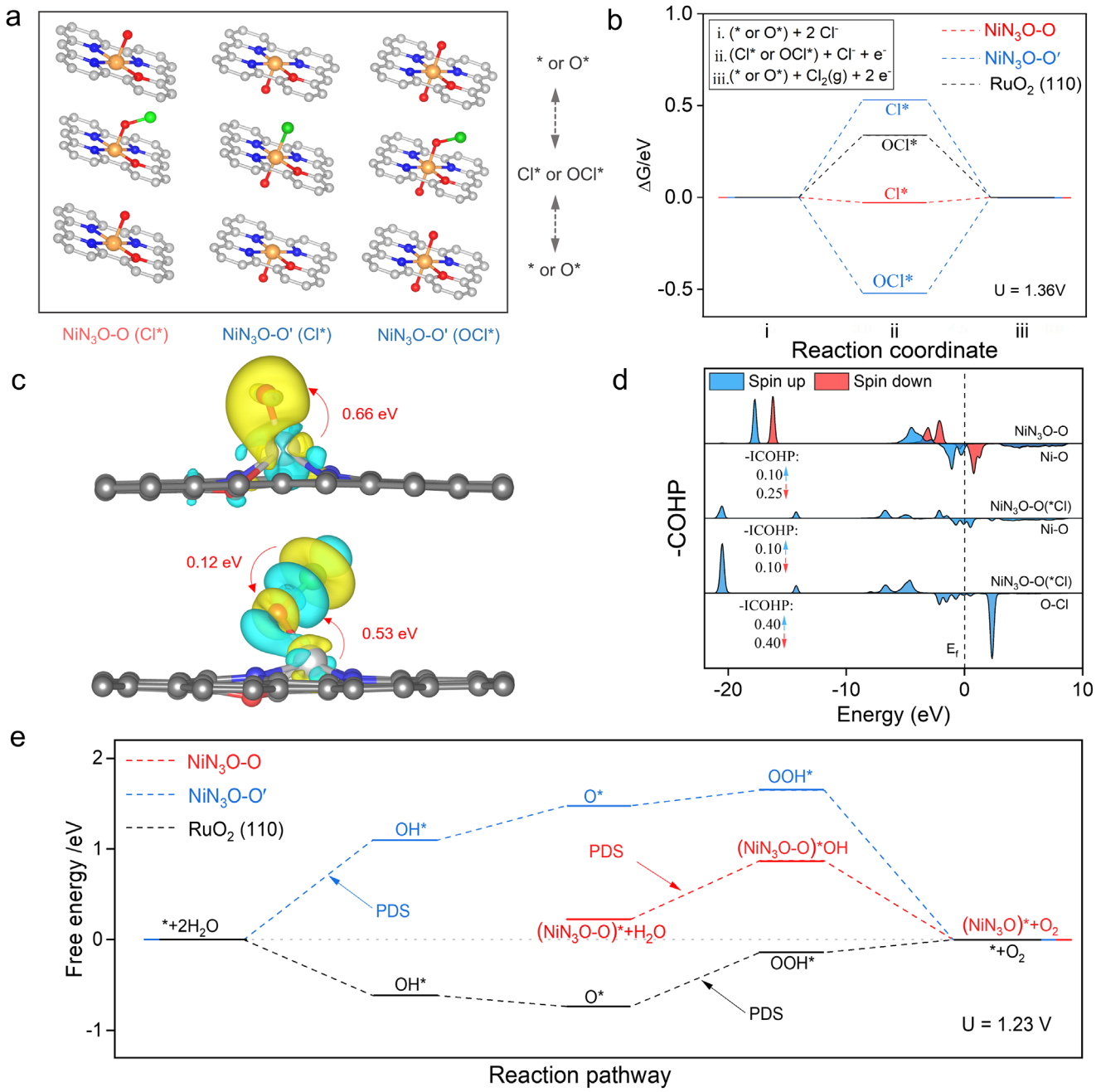

Figure 4. Theoretical analysis using DFT calculations. a) The considered CER pathways on NiN_3O-O and NiN_3O-O'. b) Gibbs free energy diagram for CER over NiN_3O-O, NiN_3O-O', and RuO_2 (110). c) Charge density difference and charge transfer before and after the Cl adsorption on NiN_3O-O. Yellow and teal colors represent charge accumulation and loss, respectively. d) Analysis of -COHP before and after the adsorption of Cl on NiN_3O-O. The integral of -COHP over the Fermi level (-ICOHP) was calculated. The upwards and downwards arrows indicate spin-up and spin-down states, respectively. e) Gibbs free energy diagram of OER over NiN_3O-O, NiN_3O-O', and RuO_2 (110).

process is most likely to proceed via the adsorption of Cl onto the O_{ot} site of the Ru_{cus} atom, resulting in the formation of an OCl* structure.[70,79] Therefore, we constructed the possible adsorption structures of NiN_3O-O, NiN_3O-O', and RuO_2 (110) under CER conditions (Figures S17–S19, Supporting Information).

Under the conditions of U = 1.36 V_{RHE}, the Gibbs free energy changes of the possible adsorbates (Cl* and OCl*) on NiN_3O-O, NiN_3O-O', and RuO_2 (110) were evaluated (Figure 4b; Figure S20, Supporting Information). The metal Ni site of NiN_3O-O' shows the largest Gibbs free energy change ($\Delta G_{Cl\text{-}I^*}$ = 0.53 eV) when it directly adsorbs Cl via the Step I (* + Cl^- →Cl* + e^-) of the Cl* path, which indicates that the metal Ni site requires a higher energy to adsorb Cl. This results in an overpotential of up to 0.53 V. The metal Ni site showed the lowest Gibbs free energy change ($\Delta G_{Cl\text{-}II^*}$ = -0.52 eV) for Cl adsorption through the OCl* pathway, indicating that the strong adsorption of Cl by the pathway would

lead to the difficulty of subsequent Cl_2 desorption. In contrast, NiN_3O-O exhibits a balanced Gibbs free energy change ($\Delta G_{Cl\text{-}I^*}$ = 0.028 eV) through the Cl* path, and its small Gibbs free energy change can easily adsorb Cl and recombine with another Cl^- in the electrolyte to form Cl_2. Therefore, the thermodynamic overpotential of CER generated by NiN_3O-O through the Cl* path is 28 mV, significantly lower than those of the Cl* pathway and OCl* pathway on NiN_3O-O' ($\eta_{td(CER\text{-}I)}$= 0.53 V and $\eta_{td(CER\text{-}II)}$= 0.52 V). This suggests that the NiN_3O-O generation through the axial O_{ot} is the most likely pathway for CER. In addition, the Gibbs free energy $\Delta G_{Cl\text{-}II^*}$ = 0.34 eV ($\eta_{td(CER\text{-}II)}$= 0.34 V) of CER catalyzed by RuO_2 (110) through the OCl* pathway is consistent with the calculation results of other literature,[25,59] indicating that the energy consumption of CER catalyzed by RuO_2 (110) is higher than that of NiN_3O-O. This is consistent with the above experimental results. The interaction between NiN_3O-O and Cl before and after adsorption was analyzed by charge density difference, charge transfer, and crystal orbital Hamilton population (COHP) (Figure 4c,d). In addition, the integral of -COHP over Fermi levels (-ICOHP) was calculated to quantitatively describe the covalent bond strength between atoms. In the case of unadsorbed Cl, the O_{ot} atom gets charge from the Ni atom, and the charge transfer is 0.66 eV, while the value of spin-down -ICOHP is 0.25, which indicates that the O_{ot} structure possesses stability. Upon adsorption of Cl, the amount of charge transferred from Ni atoms to O_{ot} atoms decreases, and the relative strength of the Ni-O covalent bond decreases somewhat. However, the charge transferred from Cl atoms to O_{ot} atoms is 0.12 eV, and the -ICOHP of its O-Cl is 0.4, indicating that the O_{ot} structure is conducive to Cl adsorption and also optimizesthr Cl adsorption energy, which is the origin of the superior CER activity of NiN_3O-O.

Previous studies have shown that the O_{ot} intermediate formed at the Ru_{cus} site of RuO_2 (110) induces CER while simultaneously triggering the side reaction OER.[80,81] Similarly, the O_{ot} site in NiN_3O-O facilitates CER while potentially serving as an O* precursor for OER. To evaluate the selectivity of NiN_3O-O for CER against OER, we investigated the Gibbs free energy changes of NiN_3O-O, NiN_3O-O', and RuO_2(110) during OER (Figure 4e; Figure S21, Supporting Information). As shown in Figure 4e, the O_{ot} site in NiN_3O-O acts as the O* precursor, and the formation of OH* and desorption of O_2 are needed to complete the OER process. The formation of OH* is defined as the potential-determining step (PDS) for the top O_{ot} site of NiN_3O-O and the bottom Ni site of NiN_3O-O', with corresponding overpotentials ($\eta_{td(OER)}$) of 0.64 and 1.08 V, respectively. In comparison, the PDS of RuO_2 (110) is the formation of OOH*, with an overpotential ($\eta_{td(OER)}$) of 0.59 V. This indicates that the upper O_{ot} site and the bottom Ni site of NiN_3O-O are intrinsically less active for OER. To further evaluate the selectivity of CER, we calculated the overpotential difference between OER and CER, defined as $\Delta\eta_{selectivity} = \eta_{td(OER)} - \eta_{td(CER)} - 0.13$. A larger $\Delta\eta_{selectivity}$ value indicates a higher selectivity of the catalyst for CER. As shown in Figure S22 (Supporting Information), the $\Delta\eta_{selectivity}$ of NiN_3O-O is 0.48 V, higher than that of NiN_3O-O' (0.45 V). This indicates that NiN_3O-O exhibits a greater selectivity for CER through its unique O_{ot} site. In contrast, RuO_2 (110) shows a $\Delta\eta_{selectivity}$ of only 0.12 V, a significantly smaller value, suggesting that RuO_2 (110) and similar MO catalysts are less likely to achieve a high CER selectivity. This conclusion is consistent with previous literature results.[82]

3. Conclusion

In summary, this study successfully designed a highly efficient non-noble metal SAC structure, NiN_3O-O, for CER by combining thermodynamic stability analysis and catalytic activity volcano based screening. As a follow-up proof-of-concept experiment, the NiN_3O-O SACs with axial O_{ot} structure were synthesized on oxidized carbon black (OCB) via a high-temperature hydrothermal-annealing method. Notably, in a 1 M NaCl acidic medium, the NiN_3O-O catalyst exhibited excellent CER performance, showing a remarkably low overpotential at a current density of 10 mA cm^{-2} and achieving over 95% Cl_2 selectivity. Charge transfer analysis and COHP calculations revealed that the O_{ot} site is the key contributor to its high catalytic activity. In addition, both the axial O_{ot} site and the underlying Ni site exhibited high adsorption energy barriers for OER intermediates, effectively suppressing the competing OER and thereby ensuring high CER selectivity. Taken together, these mechanistic and performance results establish NiN_3O–O as a feasible non-noble-metal SAC for CER. NiN_3O-O not only has excellent performance but also has significant cost advantages, showing great potential for industrial applications. Preliminary long-term cycling further demonstrates its favorable stability, and future optimization is expected to achieve even higher durability. Our combined theoretical and experimental work expands the research horizon for CER catalysts, opening a new pathway for the rational design of highly active and cost-effective CER catalysts.

Supporting Information

Supporting Information is available from the Wiley Online Library or from the author.

Acknowledgements

This work was funded by the Natural Science Foundation of Hebei (No. E2020502023) and the JSPS KAKENHI (Nos. JP25K17991, JP25K01737, and JP24K17650). The authors acknowledge the Center for Computational Materials Science, Institute for Materials Research, Tohoku University for the use of MASAMUNE-IMR (Nos. 202412-SCKXX-0211 and 202412-SCKXX-0209), and the Institute for Solid State Physics (ISSP) at the University of Tokyo for the use of their supercomputers.

Conflict of Interest

The authors declare no conflict of interest.

Data Availability Statement

The data are available upon reasonable request from Corresponding Authors. Besides, the key experimental and computational data are also available in our Digital Catalysis Platform (DigCat: www.digcat.org).

Keywords

catalytic volcano model, Chlorine evolution reaction (CER), data-driven catalyst design, NiN_3O-O SAC, single-atom catalyst (SAC)

Received: September 22, 2025
Published online:

[1] World Chlorine Council, Sustainable Progress, World Chlorine Council, https://worldchlorine.org/wp-content/uploads/2020/09/2020-WCC-Sustainability Report.pdf, (accessed: March 2021).
[2] B. Elvers, *Ullmann's Encyclopedia of Industrial Chemistry*, Verlag Chemie, Hoboken, NJ **1991**, Vol. *17*.
[3] T. Brinkmann, G. G. Santonja, F. Schorcht, S. Roudier, L. D. Sancho, *Joint Research Center EU* **2014**, *JRC91156*, 25.
[4] Y. Wang, Y. Liu, D. Wiley, S. Zhao, Z. Tang, *J. Mater. Chem. A* **2021**, *9*, 18974.
[5] W. R. Leow, Y. Lum, A. Ozden, Y. Wang, D.-H. Nam, B. Chen, J. Wicks, T.-T. Zhuang, F. Li, D. Sinton, E. H. Sargent, *Science* **2020**, *368*, 1228.
[6] J. Yang, W.-H. Li, H.-T. Tang, Y.-M. Pan, D. Wang, Y. Li, *Nature* **2023**, *617*, 519.
[7] R. K. B. Karlsson, A. Cornell, *Chem. Rev.* **2016**, *116*, 2982.
[8] H. W. Lim, D. K.i Cho, J. H. Park, S.u G. Ji, Y. J. Ahn, J. Y. Kim, C. W. Lee, *ACS Catal.* **2021**, *11*, 12423.
[9] S. Trasatti, *Electrochim. Acta* **2000**, *45*, 2377.
[10] J. G. Vos, M. T. M. Koper, *J. Electroanal. Chem.* **2018**, *819*, 260.
[11] N. Menzel, E. Ortel, K. Mette, R. Kraehnert, P. Strasser, *ACS Catal.* **2013**, *3*, 1324.
[12] S. Choi, W. I. Choi, J.-S. Lee, C. H. Lee, M. Balamurugan, A. D. Schwarz, Z. S. Choi, H. Randriamahazaka, K. T. Nam, *Adv. Mater.* **2023**, *35*, 2300429.
[13] D. Zhang, H. Li, *ChemRxiv* **2024**. https://doi.org/10.26434/chemrxiv-2024-9lpb9.
[14] I. A. Moreno-Hernandez, B. S. Brunschwig, N. S. Lewis, *Energy Environ. Sci.* **2019**, *12*, 1241.
[15] M. Košević, S. Stopic, A. Bulan, J. Kintrup, R. Weber, J. Stevanović, V. Panić, B. Friedrich, *Adv. Powder Technol.* **2017**, *28*, 43.
[16] J. Hu, H. Xu, X. Feng, L. Lei, Y. He, X. Zhang, *ChemElectroChem* **2021**, *8*, 1204.
[17] B. Xiaoyang, B. Jiqing, *J. Electrochem. Soc.* **2018**, *165*, H177.
[18] H. Qi, L. Wang, W. Sun, Z. Yang, X.u Chen, J. Yu, W. Wu, G. Liu, *Ind. Eng. Chem. Res.* **2023**, *62*, 11517.
[19] S. Wang, H. Xu, P. Yao, X. Chen, *Electrochemistry* **2012**, *80*, 507.
[20] K. Xiong, Z. Deng, L. Li, S. Chen, M. Xia, L. Zhang, X. Qi, W. Ding, S. Tan, Z. Wei, *J. Appl. Electrochem.* **2013**, *43* , 847.
[21] Y. Wang, Y. Xue, C. Zhang, *Small* **2021**, *17*, 2006587.
[22] K. Xiong, L. Peng, Y. Wang, L. Liu, Z. Deng, L. Li, Z. Wei, *J. Appl. Electrochem.* **2016**, *46*, 841.
[23] Y. Yao, L. Zhao, J. Dai, J. Wang, C. Fang, G. Zhan, Q. Zheng, W. Hou, L. Zhang, *Angew. Chem., Int. Ed.* **2022**, *61*, 202208215.
[24] J. Wang, L. Zhao, Y. Zou, J. Dai, Q. Zheng, X. Zou, L. Hu, W. Hou, R. Wang, K. Wang, Y. Shi, G. Zhan, Y. Yao, L. Zhang, *J. Am. Chem. Soc.* **2024**, *146*, 11152.
[25] Y. Liu, C. Li, C. Tan, Z. Pei, T. Yang, S. Zhang, Q. Huang, Y. Wang, Z. Zhou, X. Liao, J. Dong, H. Tan, W. Yan, H. Yin, Z.-Q. Liu, J. Huang, S. Zhao, *Nat. Commun.* **2023**, *14*, 2475.
[26] T. Lim, G. Y. Jung, J. H. Kim, S. O. Park, J. Park, Y.-T. Kim, S. J. Kang, H. Y. Jeong, S. K. Kwak, S. H. Joo, *Nat. Commun.* **2020**, *11*, 412.
[27] S. Zhao, H. Li, J. Dai, H. Li, J. Dai, Y. Jiang, G. Zhan, M. Liao, H. Sun, Y. Shi, C. Ling, Y. Yao, L. Zhang, *Nat Sustain* **2024**, *7*, 148.
[28] D. Zhang, Z. Wang, F. Liu, P. Yi, L. Peng, Y. Chen, L. Wei, H. Li, *J. Am. Chem. Soc.* **2024**, *146*, 3210.
[29] D. Zhang, Y. Hirai, K. Nakamura, K. Ito, Y. Matsuo, K. Ishibashi, Y. Hashimoto, H. Yabu, H. Li, *Chem. Sci.* **2024**, *15*, 5123.
[30] H. Cao, Q. Wang, Z. Zhang, H.-M. Yan, H. Zhao, H. B. Yang, B. Liu, J. Li, Y.-G. Wang, *J. Am. Chem. Soc.* **2023**, *145*, 13038.
[31] B. Sun, Z. Li, D. Xiao, H. Liu, K. Song, Z. Wang, Y. Liu, Z. Zheng, P. Wang, Y. Dai, B. Huang, A. Thomas, H. Cheng, *Angew. Chem., Int. Ed.* **2024**, *63*, 202318874.
[32] Y. Wang, D. Zhang, B. Sun, X. Jia, L. Zhang, H. Cheng, J. Fan, H. Li, *Angew. Chem., Int. Ed.* **2025**, *64*, 202418228.
[33] Y. Li, Z.-S. Wu, P. Lu, X. Wang, W. Liu, Z. Liu, J. Ma, W. Ren, Z. Jiang, X. Bao, *Adv. Sci.* **2020**, *7*, 1903089.
[34] W. Zang, T. Sun, T. Yang, S. Xi, M. Waqar, Z. Kou, Z. Lyu, Y. P. Feng, J. Wang, S. J. Pennycook, *Adv. Mater.* **2021**, *33*, 2003846.
[35] Z. Wang, X. Jin, C. Zhu, Y. Liu, H. Tan, R. Ku, Y. Zhang, L. Zhou, Z. Liu, S.-J. Hwang, H. J. Fan, *Adv. Mater.* **2021**, *33*, 2104718.
[36] C. Xia, Y. Qiu, Y. Xia, P. Zhu, G. King, X. Zhang, Z. Wu, J. Y. Kim, D. A. Cullen, D. Zheng, P. Li, M. Shakouri, E. Heredia, P. Cui, H. N. Alshareef, Y. Hu, H. Wang, *Nat. Chem.* **2021**, *13*, 887.
[37] C. Gu, Y. Zhang, P. He, M. Gan, J. Zhu, H. Yin, *J. Hazard. Mater.* **2024**, *472*, 134515.
[38] Y. Wu, X. Wang, B. Tian, W. Shuang, Z. Bai, L. Yang, *Inorg. Chem. Front.* **2023**, *10*, 4209.
[39] Y. Wu, C. Chen, X. Yan, X. Sun, Q. Zhu, P. Li, Y. Li, S. Liu, J. Ma, Y. Huang, B. Han, *Angew. Chem., Int. Ed.* **2021**, *60*, 20803.
[40] Q. Jin, C. Wang, Y. Guo, Y. Xiao, X. Tan, J. Chen, W. He, Y. Li, H. Cui, C. Wang, *Adv. Sci.* **2023**, *10*, 2302152.
[41] C. Liu, H. Li, F. Liu, J. Chen, Z. Yu, Z. Yuan, C. Wang, H. Zheng, G. Henkelman, L. Wei, Y. Chen, *J. Am. Chem. Soc.* **2020**, *142*, 21861.
[42] W. Yang, B. Zhou, Z. Jia, C. Wu, L. Wei, Z. Gao, H. Li, *ChemCatChem* **2022**, *14*, 202201016.
[43] C. Liu, Z. Yu, F. She, J. Chen, F. Liu, J. Qu, J. M. Cairney, C. Wu, K. Liu, W. Yang, H. Zheng, Y. Chen, H. Li, L. Wei, *Energy Environ. Sci.* **2023**, *16*, 446.
[44] M. Ha, P. Thangavel, N. K. Dang, D. Y. Kim, S. Sultan, J. S. Lee, K. S. Kim, *Small* **2023**, *19*, 2300240.
[45] S. Choung, H. Yang, J. Moon, W. Park, H. June, C. Lim, J. W. Han, *Catal. Today* **2024**, *425*, 114358.
[46] J. Liu, J. J. Hinsch, H. Yin, P. Liu, H. Zhao, Y. Wang, *J. Electroanal. Chem.* **2022**, *907*, 116071.
[47] Q. Zhang, J. Guan, *Adv. Funct. Mater.* **2020**, *30*, 2000768.
[48] J. Su, L. Zhuang, S. Zhang, Q. Liu, L. Zhang, G. Hu, *Chin. Chem. Lett.* **2021**, *32*, 2947.
[49] A. Cho, B. J. Park, J. W. Han, *Front. Chem.* **2022**, *10*, 873609.
[50] Y. Wang, R. Huang, J. W. Han, *J. Phys. D, Appl. Phys.* **2022**, *55*, 323001.
[51] Y. Mun, S. Lee, K. Kim, S. Kim, S. Lee, J. W. Han, J. Lee, *J. Am. Chem. Soc.* **2019**, *141*, 8b13543.
[52] E. Jung, H. Shin, B.-H. Lee, V. Efremov, S. Lee, H. S. Lee, J. Kim, W. Hooch Antink, S. Park, K.-S. Lee, S.-P. Cho, J. S. Yoo, Y.-E. Sung, T. Hyeon, *Nat. Mater.* **2020**, *19*, 436.
[53] W. Yang, S. Xu, K. Ma, C. Wu, I. D. Gates, X. Ding, W. Meng, Z. Gao, *Nano Mater. Sci.* **2020**, *2*, 120.
[54] I. Sohrabnejad-Eskan, A. Goryachev, K. S. Exner, L. A. Kibler, E. J. M. Hensen, J. P. Hofmann, H. Over, *ACS Catal.* **2017**, *7*, 2403.
[55] N. L. Dashti, A. Mohajeri, *Int. J. Hydrogen Energy* **2023**, *48*, 2973.
[56] L. Quan, X. Zhao, L.-M. Yang, B. You, B. Y. Xia, *Angew. Chem., Int. Ed.* **2025**, *64*, 202414202.
[57] K. S. Exner, *ChemElectroChem* **2019**, *6*, 3401.
[58] V. Sumaria, D. Krishnamurthy, V. Viswanathan, *ACS Catal.* **2018**, *8*, 9034.
[59] J. Yang, W.-H. Li, K. Xu, S. Tan, D. Wang, Y. Li, *Angew. Chem.* **2022**, *134*, 202200366.
[60] H. A. Hansen, I. C. Man, F. Studt, F. Abild-Pedersen, T. Bligaard, J. Rossmeisl, *Phys. Chem. Chem. Phys.* **2010**, *12*, 283.
[61] P. Sabatier, *Ber. Dtsch. Chem. Ges.* **1911**, *44*, 1984.
[62] J. K. Nørskov, J. Rossmeisl, A. Logadottir, L. R. K. J. Lindqvist, J. R. Kitchin, T. Bligaard, H. Jonsson, *J. Phys. Chem. B* **2004**, *108*, 17886.
[63] M. Pourbaix, *Atlas of Electrochemical Equilibria in Aqueous Solutions NACE*, **1966**.
[64] K. S. Exner, *ChemSusChem* **2019**, *12*, 2330.
[65] S. Trasatti, *Electrochim. Acta* **1987**, *32*, 369.
[66] H. A. Hansen, J. Rossmeisl, J. K. Nørskov, *Phys. Chem. Chem. Phys.* **2008**, *10*, 3722.

[67] T. Lim, J. H. Kim, J. Kim, D. S. Baek, T. J. Shin, H. Y. Jeong, K.-S. Lee, K. S. Exner, S. H. Joo, *ACS Catal.* **2021**, *11*, 12232.
[68] Z. Liu, B. Zhang, Y. Liu, C. Wang, C. Ye, W. Yang, *J. Mater. Chem. A* **2025**, *13*, 10683.
[69] B. Yue, L. Lin, Y. Lei, H. Xie, Y. Si, Q. Yang, X. Liu, *ACS Appl. Mater. Interfaces* **2023**, *15*, 33665.
[70] K. S. Exner, J. Anton, T. Jacob, H. Over, *Angew. Chem., Int. Ed.* **2016**, *55*, 7501.
[71] T. Shinagawa, A. T. Garcia-Esparza, K. Takanabe, *Sci. Rep.* **2015**, *5*, 13801.
[72] K. S. Exner, J. Anton, T. Jacob, H. Over, *Electrochim. Acta* **2014**, *120*, 460.
[73] V. Petrykin, K. Macounova, O. A. Shlyakhtin, P. Krtil, *Angew. Chem.* **2010**, *122*, 4923.
[74] G. Raj, R. Nandan, K. Kumar, D. B. Gorle, A. B. Mallya, S. M. Osman, J. Na, Y. Yamauchi, K. K. Nanda, *Mater. Horiz.* **2023**, *10*, 5032.
[75] L. Cai, Y. Liu, J. Zhang, Q. Jia, J. Guan, H. Sun, Y. Yu, Y. Huang, *J. Energy Chem.* **2024**, *92*, 95.
[76] C. E. Finke, S. T. Omelchenko, J. T. Jasper, M. F. Lichterman, C. G. Read, N. S. Lewis, M. R. Hoffmann, *Energy Environ. Sci.* **2019**, *12*, 358.
[77] R. R. Rao, M. J. Kolb, N. B. Halck, A. F. Pedersen, A. Mehta, H. You, K. A. Stoerzinger, Z. Feng, H. A. Hansen, H. Zhou, L. Giordano, J. Rossmeisl, T. Vegge, I. Chorkendorff, I. E. L. Stephens, Y. Shao-Horn, *Energy Environ. Sci.* **2017**, *10*, 2626.
[78] R. R. Rao, M. J. Kolb, L. Giordano, A. F. Pedersen, Y.u Katayama, J. Hwang, A. Mehta, H. You, J. R. Lunger, H. Zhou, N. B. Halck, T. Vegge, I.b Chorkendorff, I. E. L. Stephens, Y. Shao-Horn, *Nat. Catal.* **2020**, *3*, 516.
[79] K. S. Exner, J. Anton, T. Jacob, H. Over, *Angew. Chem.* **2014**, *126*, 11212.
[80] J. Rossmeisl, Z.-W. Qu, H. Zhu, G.-J. Kroes, J. K. Nørskov, *J. Electroanal. Chem.* **2007**, *607*, 83.
[81] Y.-H. Fang, Z.-P. Liu, *J. Am. Chem. Soc.* **2010**, *132*, 18214.
[82] S. Li, X. Guo, X. Liu, J. Shui, *ACS Catal.* **2024**, *14*, 1962.